Technical Notes

Formation of Bifurcated Wakes Behind Finite Span Flapping Wings

Meilin Yu* and Z. J. Wang†
University of Kansas, Lawrence, Kansas 66045
and
Hui Hu‡
Iowa State University, Ames, Iowa 50011

Nomenclature

C	=	chord length, m
C_T	=	thrust coefficient
f	=	flapping frequency, Hz
h_{tip}	=	plunge amplitude at the wing tip, m
k	=	$\omega C/U_\infty$, reduced frequency
l_{span}	=	wingspan, m
Re	=	$U_\infty C/\nu$, Reynolds number
r_z	=	z-directional distance away from the wing tip, m
S_{wing}	=	wing area, m²
St	=	$f h_{tip}/U_\infty$, Strouhal number
U_∞	=	freestream velocity, m/s
ν	=	kinematic viscosity of fluid, m²/s
α, α_0	=	pitch angle of the airfoil and initial pitch angle, respectively, deg
ϕ, ϕ_0	=	phase angle and initial phase angle, respectively, rad
ω	=	angular frequency, rad/s
ω_z	=	spanwise (z direction) vorticity

I. Introduction

Flapping wings with low aspect ratios (≤ 6) are beneficial for agile locomotion. According to Shyy et al. [1] and Ringuette et al. [2], most insects have these types of wings. As flying insects are usually adopted as the prototype for future micro air vehicles, a thorough understanding on the aerodynamic performance of low-aspect-ratio wings becomes necessary. Some studies [2–11] have already been carried out to investigate the unsteady aerodynamics of low-aspect-ratio wings. An analysis of the flow vortex structures is one of the most important means to paint an intuitive picture on the vortex topology, and can help distinguish the flow features contributing to the aerodynamic performance of the flapping wings.

*Postdoctoral Researcher, Department of Aerospace Engineering; mlyu@ku.edu. Member AIAA.

†Spahr Professor and Chair, Department of Aerospace Engineering. Associate Fellow AIAA.

‡Associate Professor, Department of Aerospace Engineering. Associate Fellow AIAA.

Dye flow visualization was used by von Ellenrieder et al. [4] to investigate the three-dimensional (3-D) flow structure of a finite span low-aspect-ratio flapping wing with two free ends. The flow structure of merged vortex rings, which were formed by the leading and trailing vortices shed each half-flapping cycle, was identified from their study. Vorticity-reconnection phenomena were reported from the numerical results by Blondeaux et al. [5] with the same geometric configuration and dimensionless parameters as those in the experiment aforementioned. The results from their numerical simulations reproduced the main flow features shown in the experiment. Buchholz and Smits [6] experimentally examined the vortex structure around a pitching panel with a very low aspect ratio, and found that the wake was dominated by vortex loops of alternating signs. They also indicated that, as the Strouhal number increased, two separate trains of vortex structures expanding in the transverse direction showed up. Similar results have been displayed by Dong et al. [7] almost at the same time. They computed the flow field generated by a finite span flapping wing with two free ends and a low aspect ratio as well, but of elliptical planform and cross section. The bifurcated wake topology, which consisted of two trains of vortex rings departing from each other in the transverse direction, was reported, and this phenomenon was closely related to the formation of distinct vortex rings evolved from two sets of shed interconnected vortex loops. Recently, Hu et al. [10] used particle image velocimetry to examine the flow field behind a root-fixed flapping wing with a low aspect ratio. A bifurcated wake structure was found to appear in the region near the wing tip. Dewey et al. [11] found that the bifurcated vortex-array configuration also existed in the wake of a batoid-inspired oscillating fin, and was closely related with the Strouhal number and the wavelength of the chordwise traveling wave motion. From all these previous studies, it seems that the bifurcated vortex topology around the finite span flapping wings is quite robust, and a thorough explanation of its formation mechanism is needed.

The present paper attempts to explain the formation of bifurcated wakes via the detailed vortex-structure analyses based on the numerical results from a high-order accurate flow solver. High-order methods have been shown to be more accurate than low-order counterparts for vortex-dominated flows due to their prominent low-dissipation features [12]. Herein, a 3-D unstructured dynamic-grid spectral-difference (SD) Navier–Stokes flow solver developed by Yu et al. [13] is adopted to carry out the simulations.

The paper is further organized as follows. In Sec. II, the dynamic-grid SD method and simulation setup are briefly described. Then, numerical results are presented, and bifurcated wake topology is discussed in Sec. III. Finally, conclusions are summarized in Sec. IV.

II. Numerical Methods and Simulation Parameters

A. Governing Equations and Space Discretization

A 3-D high-order SD solver for dynamic grids is used for the present simulations. The numerical method will be briefed as follows for completeness, and the reader is referred to the previous work by Yu et al. [13] for details.

We consider the unsteady compressible Navier–Stokes equations in conservation form in the physical domain (t, x, y, z)

$$\frac{\partial Q}{\partial t} + \frac{\partial F}{\partial x} + \frac{\partial G}{\partial y} + \frac{\partial H}{\partial z} = 0 \qquad (1)$$

Herein, $Q = (\rho, \rho u, \rho v, \rho w, E)^T$ are the conservative variables; ρ is the fluid density; u, v, and w are the Cartesian velocity components; and E is the total internal energy. F, G, and H are the total fluxes, including both the inviscid and viscous flux vectors in the x, y, and z directions. On assuming that the fluid obeys the perfect-gas

law, the pressure is related to the total internal energy by $E = p/(\gamma - 1) + 1/2\rho(u^2 + v^2 + w^2)$, which closes the solution system.

To achieve an efficient implementation, a time-dependent coordinate transformation from the physical domain (t, x, y, z) to the computational domain (τ, ξ, η, ζ) is applied to Eq. (1), and we obtain

$$\frac{\partial \tilde{Q}}{\partial \tau} + \frac{\partial \tilde{F}}{\partial x} + \frac{\partial \tilde{G}}{\partial y} + \frac{\partial \tilde{H}}{\partial z} = 0 \qquad (2)$$

in which

$$\begin{cases} \tilde{Q} = |J|Q \\ \tilde{F} = |J|(Q\xi_\tau + F\xi_x + G\xi_y + H\xi_z) \\ \tilde{G} = |J|(Q\eta_\tau + F\eta_x + G\eta_y + H\eta_z) \\ \tilde{H} = |J|(Q\zeta_\tau + F\zeta_x + G\zeta_y + H\zeta_z) \end{cases} \qquad (3)$$

Herein, $\tau = t$, and $(\xi, \eta, \zeta) \in [-1, 1]^3$ are the local coordinates in the computational domain. In the transformation shown previously, the Jacobian matrix J takes the following form:

$$J = \frac{\partial(x, y, z, t)}{\partial(\xi, \eta, \zeta, \tau)} = \begin{pmatrix} x_\xi & x_\eta & x_\zeta & x_\tau \\ y_\xi & y_\eta & y_\zeta & y_\tau \\ z_\xi & z_\eta & z_\zeta & z_\tau \\ 0 & 0 & 0 & 1 \end{pmatrix} \qquad (4)$$

Note that all the information concerning grid velocity $\mathbf{v}_g = (x_\tau, y_\tau, z_\tau)$ is related with (ξ_t, η_t, ζ_t) by

$$\begin{cases} \xi_t = -\mathbf{v}_g \cdot \nabla\xi \\ \eta_t = -\mathbf{v}_g \cdot \nabla\eta \\ \zeta_t = -\mathbf{v}_g \cdot \nabla\zeta \end{cases} \qquad (5)$$

The SD method is used for the space discretization. In this method, two sets of points, namely, the solution and flux points are given in one element. The solution points are chosen as the Chebyshev–Gauss quadrature points, and the flux points are selected to be the Legendre–Gauss points with end points as -1 and 1, considering stability issues. Conservative variables are defined at the solution points, and then interpolated to flux points using Lagrange polynomials to calculate local fluxes. To ensure conservation, the approximate Riemann solver and the Bassi-Rebay 1 approach [14] are used to reconstruct the common inviscid and viscous fluxes on the element interfaces, respectively. Because the flow regime for flapping flight is almost incompressible in nature and the present governing equations are compressible Navier–Stokes equations, the AUSM$^+$-up Riemann solver [15] for all speeds is selected to ensure good performance of the solver at low Mach numbers.

B.   Problem Statement and Parameter Setup

The finite span rectangular flapping wing, as shown in Fig. 1, is studied here. Grids on the wing surface and on the root plane are displayed in Fig. 1 as well. Note that, in the simulations, the root plane is set to be symmetric to save computational cost. A medium mesh and a third-order accurate SD space discretization are adopted in the simulations to reconcile the competing factors of flow resolution and computational cost. In addition, time integration is performed with the explicit three-stage total-variation-diminishing Runge–Kutta method.

Two types of flapping-wing kinematics are considered here. The first type is the root-fixed plunging motion. The other type is the linearly combined plunging and pitching motions. The corresponding grid-deformation strategies for these two types of motions are specified as follows.

The root-fixed plunging motion for one particular point (x, y, z) on the flapping wing with the initial position (x_i, y_i, z_i) is governed by the functions as follows:
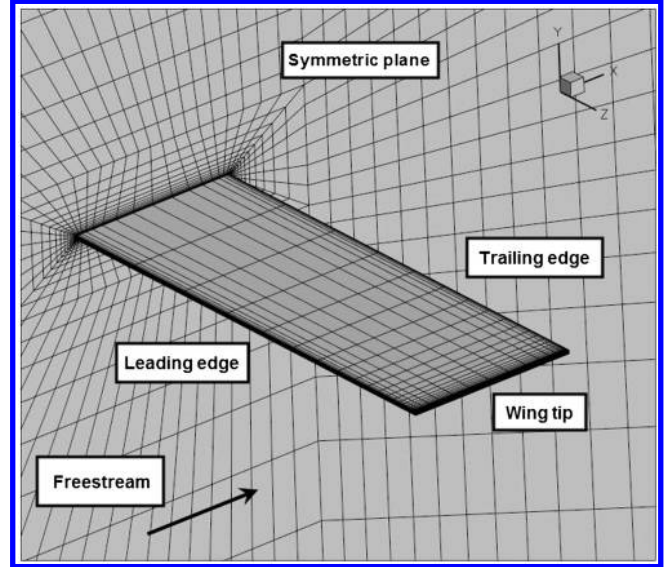

Fig. 1   Meshes and the computational configuration for the rectangular wing.

$$x = x_i, \qquad y = y_i + h_i \sin(\omega t), \qquad z = z_i \qquad (6)$$

in which h_i is determined from the parabola $h_i = h_{\text{tip}}(1 - r_z/l_{\text{span}})^2$, with h_{tip} the desired plunge amplitude on the wing tip, l_{span} the wingspan, and r_z the z-directional distance away from the wing tip.

The pitching motion for the same point aforementioned is controlled by the following rotational transformation as

$$\begin{pmatrix} x_{\text{present}} - x_{i,c} \\ y_{\text{present}} - y_{i,c} \end{pmatrix} = \begin{pmatrix} \cos(\Delta\alpha) & -\sin(\Delta\alpha) \\ \sin(\Delta\alpha) & \cos(\Delta\alpha) \end{pmatrix} \begin{pmatrix} x_{\text{former}} - x_{i,c} \\ y_{\text{former}} - y_{i,c} \end{pmatrix} \qquad (7)$$

with the pivot $x_{i,c} = \text{const}$, $y_{i,c} = h_{i,c} \sin(\omega t)$, and the pitching angle $\alpha = \alpha_0 \sin(\omega t + \phi_0)$. Herein, the phase lag ϕ_0 between the plunging and pitching motions is set as $5\pi/12$ according to the suggestions from Anderson et al. [16]. The combined motion is the linear combination of the root-fixed plunging motion and the pitching motion. After the wing-surface deformation is specified, a polynomial-blending function is used to determine the movement of other grid points. Details can be found in [13].

The Strouhal number ($St = fh_{\text{tip}}/U_\infty$) is selected to be 0.38 based on the definition in [17]. Herein, $f = \omega/2\pi$ is the flapping frequency, and U_∞ is the freestream velocity. The chosen value of the Strouhal number falls well into the optimal range usually adopted by flying insects, birds, and swimming fish (i.e., $0.2 < St < 0.4$). The reduced frequency ($k = \omega C/U_\infty$) based on the angular flapping frequency and the chord length is set as 3.5. The Reynolds number ($Re = U_\infty C/\nu$) based on the freestream velocity and the chord length is 1200. The aspect ratio ($l_{\text{span}}^2/S_{\text{wing}}$), which is the ratio between the square of the wingspan (l_{span}) and the wing area (S_{wing}), is set as 2.6772. The wing thickness over the chord length is 0.02. All these parameters are selected based on the experimental setup stated in [10]. The Mach number of the freestream is set to be 0.05, under which the flow is almost incompressible.

III.   Numerical Results and Discussions

A.   Comparison with Experimental Results

The wake vortex structures of the root-fixed plunging rectangular wing at phase angle $\phi = 0$ from the perspective view are shown in Fig. 2a. In this figure, the vortical structures are indicated by the iso-Q surfaces ($Q = 0.05$) colored with streamwise velocity. The Q-criterion is a Galilean-invariant vortex criterion, which is defined as follows [18]:

$$Q = \frac{1}{2}(R_{ij}R_{ij} - S_{ij}S_{ij}) = -\frac{1}{2}\frac{\partial u_i}{\partial x_j}\frac{\partial u_j}{\partial x_i} \qquad (8)$$

in which $R_{ij} = 1/2[(\partial u_i/\partial x_j) - (\partial u_j/\partial x_i)]$ is the angular rotation tensor, and $S_{ij} = 1/2[(\partial u_i/\partial x_j) + (\partial u_j/\partial x_i)]$ is the rate-of-strain tensor. Different vortices have been marked out with rectangular windows or solid arrows, which indicate the rotation directions. It is clear from the figure that the complex vortex system around the flapping wing can be decomposed into four parts, namely, leading-edge vortices (LEVs), trailing-edge vortices (TEVs), tip vortices (TVs), and entangled vortices due to the interaction among LEVs, TEVs, and TVs. Similar wake phenomena have been reported by other researchers [5,7] for free-end finite span wings.

The time-averaged velocity fields at 75% wingspan from both the numerical simulations and the experimental results [10] are displayed in Figs. 2b and 2c. Note that all contour levels in the numerical simulations are kept the same as those in the experiment. The wake region from the numerical simulation corresponds to the wake region from the experimental results, as indicated by the frame. It is clear from the comparison that the numerical simulations capture the main features of the bifurcated wake indicated by experimental measurements reasonably well. Here, it should be mentioned that in [10], there exists some piezoelectric material, which was used to actuate the flapping wing, between the wing root and the wind-tunnel wall. In the numerical simulations, as aforementioned, the root plane is modeled as a symmetric plane, which neglects the viscous effects of the wind-tunnel wall. From the preceding comparison, it is found that the major wake topology will not be affected by neglecting the viscous wall effects.

B. Bifurcated Wake Topology

The side and perspective views of the vortex structures of the plunging and pitching rectangular wings at phase angle $\phi = 0$ are displayed in Fig. 3. Different vortices have been marked out with solid arrows, which indicate the rotation directions. Herein, a detailed observation of the bifurcated jet effects is shown in Fig. 3b. This figure shows the 3-D vortical structures indicated by the iso-Q surfaces ($Q = 0.05$) and the spanwise vorticity field at the 75% wingspan. The trajectories of both clockwise ($-$) and anticlockwise ($+$) vortices are also schematically plotted in the figure. Note that the jet bifurcation position is determined by examining the starting point of the bifurcated wake patterns from the time-averaged velocity fields at 75% wingspan, as shown in Fig. 4b.

It has been reported in [7] that the formation of the bifurcated wake patterns behind the flapping wing is closely related to the existence of TVs. But the formation process of the bifurcated jet was not fully analyzed. Here, the formation of the bifurcated wake topology is explained via the vortex-structure analysis as follows. From Fig. 3b, it is obvious that the upper branch of the bifurcated jet is formed by an anticlockwise vortex row consisting of TEVs and a clockwise vortex row consisting of TVs, whereas the lower branch of the bifurcated jet is formed by an anticlockwise vortex row consisting of TVs and a clockwise vortex row consisting of TEVs. The reasons why TVs can contribute to the spanwise vorticity are specified as follows. Let us
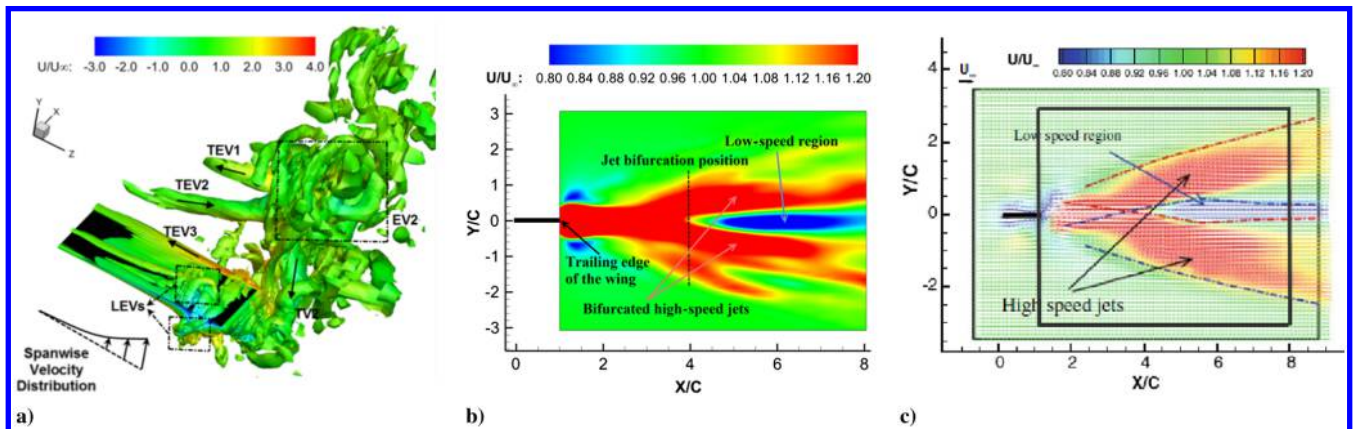

Fig. 2 Flow fields around the wing with a root-fixed plunging motion.
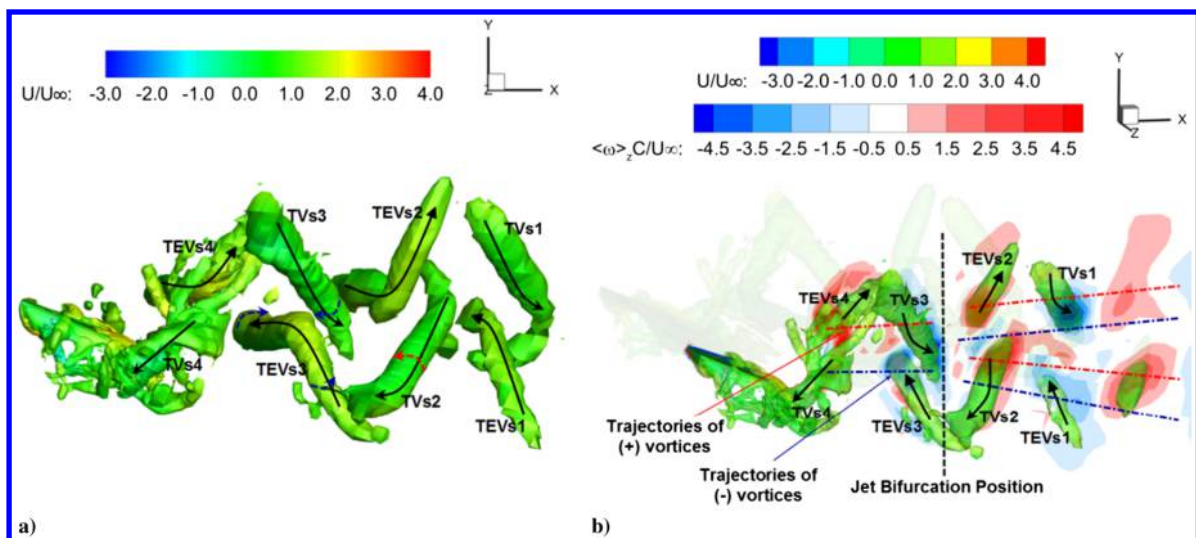

Fig. 3 Vortex topology and vorticity fields around the wing with combined motion.
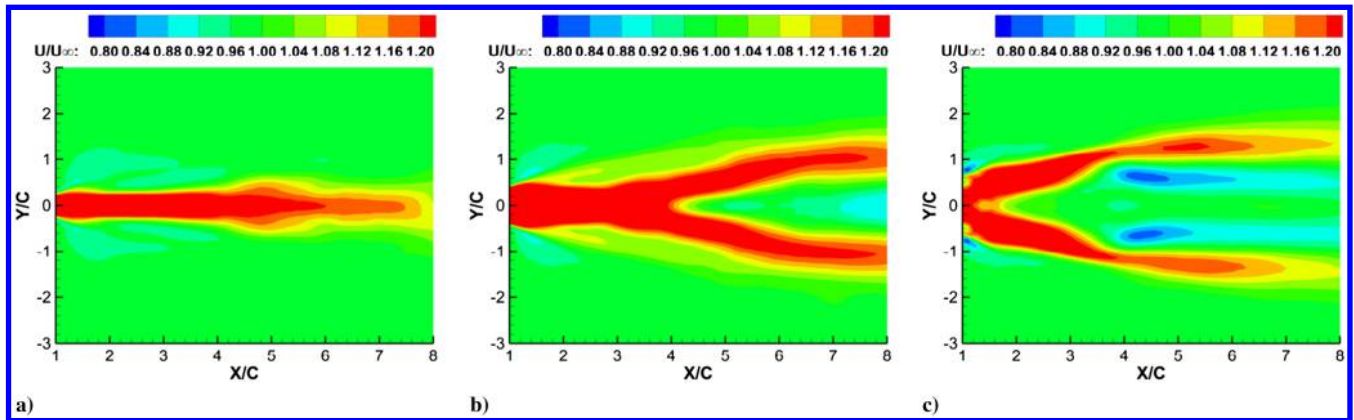
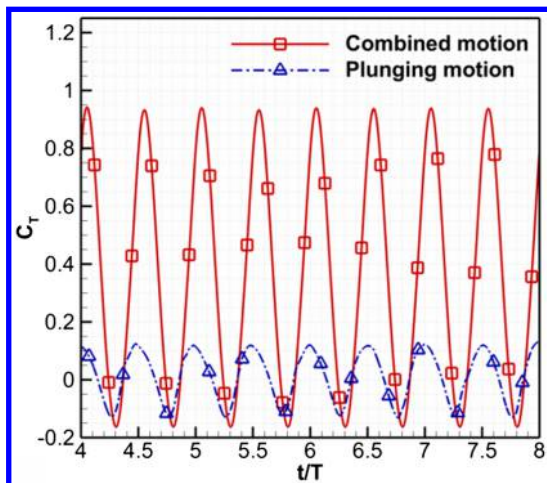Fig. 4   Time-averaged velocity fields at a) 50%, b) 75%, and c) 100% wingspan with a combined motion.

Fig. 5   Thrust-coefficient histories for the wing with the combined and the root-fixed plunging motions.

use TVs2, TEVs3, and TVs3 in Fig. 3a to explain the process. Because of the existence of the TVs2, the end part of the TEVs3 near the wing tip will be dragged gradually from the z direction to the y direction during the flapping stroke. This indicates that a certain amount of vorticity in the vertical (y) direction is generated. The corresponding rotation direction of the induced velocity field is schematically denoted with the dashed arrow, as drawn on the bottom end of the TEVs3. This velocity field will bend the bottom end of the TVs3 toward the TEVs2. Thus, a vorticity component in the spanwise (z) direction is induced in the TVs3. It is not hard to examine that this induced vorticity component is negative, as denoted with the dashed arrow near the bottom part of the TVs3. This explains the formation of the spanwise vorticity contribution from the TVs, and further elucidates the formation of the bifurcated wake patterns. Similar explanations can be applied to the formation of the wake pattern at the wing tip, as shown in Fig. 4c.

From the time-averaged velocity fields at different wingspan locations of the plunging and pitching wings in Fig. 4, it is observed that the thrust-indicative wake pattern (jet flow) appears on all examined sections. This implies that the net effects of the plunging and pitching motions will contribute to the thrust production on the flapping wing. This is confirmed by the thrust-coefficient history shown in Fig. 5 for the plunging and pitching wings. In this figure, the thrust-coefficient history for the root-fixed plunging motion is displayed as well. From the comparison, it is clear that the combined plunging and pitching motions with suitable phase lag is more conducive for the thrust production than the root-fixed plunging motion. In addition, it is found that the time history of the thrust coefficient for the root-fixed plunging motion exhibits certain aperiodic features. This is closely related to the unsteady flow

featured by a large amount of small vortex structures, as shown in Fig. 2a.

IV.   Conclusions

A three-dimensional high-order unstructured dynamic-grid spectral-difference Navier–Stokes flow solver is used to investigate the wake structures of the finite span flapping wings. The numerical results for the root-fixed plunging wing agree qualitatively with the experimental measurement. The formation process of the bifurcated wake topology behind the finite span flapping wing is found to be closely related to the interaction between trailing-edge vortices (TEVs) and tip vortices (TVs). The key mechanism is attributed to the fact that the rotational direction of TVs is subject to change during the interaction with TEVs.

References

[1] Shyy, W., Lian, Y., Tang, J., Viieru, D., and Liu, H., *Aerodynamics of Low Reynolds Number Flyers*, Cambridge Univ. Press, New York, 2008, pp. 18–19.

[2] Ringuette, M. J., Milano, M., and Gharib, M., "Role of the Tip Vortex in the Force Generation of Low-Aspect-Ratio Normal Flat Plates," *Journal of Fluid Mechanics*, Vol. 581, June 2007, pp. 453–468.
   doi:10.1017/S0022112007005976

[3] Shyy, W., Aono, H., Chimakurth, S. K., Trizila, P., Kang, C. K., Cesnik, C. E. S., and Liu, H., "Recent Progress in Flapping Wing Aerodynamics and Aeroelasticity," *Progress in Aerospace Sciences*, Vol. 46, No. 7, 2010, pp. 284–327.
   doi:10.1016/j.paerosci.2010.01.001

[4] von Ellenrieder, K. D., Parker, K., and Soria, J., "Flow Structures Behind a Heaving and Pitching Finite-Span Wing," *Journal of Fluid Mechanics*, Vol. 490, Sept. 2003, pp. 129–138.
   doi:10.1017/S0022112003005408

[5] Blondeaux, P., Fornarelli, F., Guglielmini, L., Triantafyllou, M. S., and Verzicco, R., "Numerical Experiments on Flapping Foils Mimicking Fish-Like Locomotion," *Physics of Fluids*, Vol. 17, No. 11, 2005, pp. 113601–113612.
   doi:10.1063/1.2131923

[6] Buchholz, J. H. J., and Smits, A. J., "On the Evolution of the Wake Structure Produced by a Low-Aspect-Ratio Pitching Panel," *Journal of Fluid Mechanics*, Vol. 564, Dec. 2005, pp. 433–443.
   doi:10.1017/S0022112005006865

[7] Dong, H. B., Mittal, R., and Najjar, F., "Wake Topology and Hydrodynamic Performance of Low Aspect-Ratio Flapping Foils," *Journal of Fluid Mechanics*, Vol. 566, Nov. 2006, pp. 309–343.
   doi:10.1017/S002211200600190X

[8] Shyy, W., and Liu, H., "Flapping Wings and Aerodynamic Lift: The Role of Leading-Edge Vortices," *AIAA Journal*, Vol. 45, No. 12, 2007, pp. 2817–2819.
   doi:10.2514/1.33205

[9] Shyy, W., Trizila, P., Kang, C., and Aono, H., "Can Tip Vortices Enhance Lift of a Flapping Wing?" *AIAA Journal*, Vol. 47, No. 2, 2009, pp. 289–293.
   doi:10.2514/1.41732

[10] Hu, H., Clemons, L., and Igarashi, H., "An Experimental Study of the Unsteady Vortex Structures in the Wake of a Root-Fixed Flapping

Wing," *Experiments in Fluids*, Vol. 51, No. 2, 2011, pp. 347–359.
doi:10.1007/s00348-011-1052-z

[11] Dewey, P. A., Carriou, A., and Smits, A. J., "On the Relationship Between Efficiency and Wake Structure of a Batoid-Inspired Oscillating Fin," *Journal of Fluid Mechanics*, Vol. 691, Jan. 2012, pp. 245–266.
doi:10.1017/jfm.2011.472

[12] Visbal, M. R., and Gaitonde, D. V., "On the Use of High-Order Finite-Difference Schemes on Curvilinear and Deforming Meshes," *Journal of Computational Physics*, Vol. 181, No. 1, 2002, pp. 155–185.
doi:10.1006/jcph.2002.7117

[13] Yu, M. L., Wang, Z. J., and Hu, H., "A High-Order Spectral Difference Method for Unstructured Dynamic Grids," *Computers and Fluids*, Vol. 48, No. 1, 2011, pp. 84–97.
doi:10.1016/j.compfluid.2011.03.015

[14] Bassi, F., and Rebay, S., "A High-Order Accurate Discontinuous Finite Element Method for the Numerical Solution of the Compressible Navier–Stokes Equations," *Journal of Computational Physics*, Vol. 131, No. 2, 1997, pp. 267–279.
doi:10.1006/jcph.1996.5572

[15] Liu, M. S., "A Sequel to AUSM, Part II: AUSM+-Up for all Speeds," *Journal of Computational Physics*, Vol. 214, No. 1, 2006, pp. 137–170.
doi:10.1016/j.jcp.2005.09.020

[16] Anderson, M., Streitlien, K., Barrett, D. S., and Triantafyllo, M. S., "Oscillating Foils of High Propulsive Efficiency," *Journal of Fluid Mechanics*, Vol. 360, April 1998, pp. 41–72.
doi:10.1017/S0022112097008392

[17] Taylor, G. K., Nudds, R. L., and Thomas, A. L. R., "Flying and Swimming Animals Cruise at a Strouhal Number Tuned for High Power Efficiency," *Nature*, Vol. 425, Oct. 2003, pp. 707–711.
doi:10.1038/nature02000

[18] Jeong, J., and Hussain, F., "On the Identification of a Vortex," *Journal of Fluid Mechanics*, Vol. 285, Feb. 1995, pp. 69–94.
doi:10.1017/S0022112095000462

S. Fu
Associate Editor

This article has been cited by:

1. Naresh Poudel, Arjun Trivedi, Parham Oveissi, Meilin Yu, Ankit Goel, John T. Hrynuk. Learning-based Adaptive Gust Mitigation with Oscillating Wings . [Abstract] [PDF] [PDF Plus]

2. Naresh Poudel, Meilin Yu, Zachary F. Smith, John T. Hrynuk. A combined experimental and computational study of a vertical gust generator in a wind tunnel . [Citation] [PDF] [PDF Plus]

3. Muhammad Saif Ullah Khalid, Imran Akhtar, Haibo Dong, Nida Ahsan, Xiaoping Jiang, Binxin Wu. 2018. Bifurcations and route to chaos for flow over an oscillating airfoil. *Journal of Fluids and Structures* **80**, 262-274. [Crossref]

4. Meilin Yu, Bin Wang, Z.J. Wang, Saeed Farokhi. 2018. Evolution of vortex structures over flapping foils in shear flows and its impact on aerodynamic performance. *Journal of Fluids and Structures* **76**, 116-134. [Crossref]

5. Shizhao Wang, Xing Zhang, Guowei He, Tianshu Liu. 2015. Evaluation of Lift Formulas Applied to Low-Reynolds-Number Unsteady Flows. *AIAA Journal* **53**:1, 161-175. [Abstract] [Full Text] [PDF] [PDF Plus]

6. Meilin Yu, Zhi J. Wang, Saeed Farokhi. Impact of Mean Flow Shear on the Wake Vortical Structure behind Oscillating Airfoils . [Citation] [PDF] [PDF Plus]

7. Shizhao Wang, Xing Zhang, Guowei He, Tianshu Liu. 2014. Lift enhancement by dynamically changing wingspan in forward flapping flight. *Physics of Fluids* **26**:6, 061903. [Crossref]